


Conductance based machine learning of optimal gate voltages for disordered Majorana wiresMatthias Thamm  and Bernd Rosenow*Institut für Theoretische Physik, Universität Leipzig, 04103 Leipzig, Germany* (Received 4 June 2023; revised 21 December 2023; accepted 22 December 2023; published 17 January 2024)

Majorana zero modes in superconductor-nanowire hybrid structures are a promising candidate for topologically protected qubits with the potential to be used in scalable structures. Currently, disorder in such Majorana wires is a major challenge, as it can destroy the topological phase and thus reduce the yield in the fabrication of Majorana devices. We study machine learning optimization of a gate array in proximity to a grounded Majorana wire, which allows us to reliably compensate even strong disorder. We propose a metric for optimization which can be implemented based on measurements of the nonlocal conductance through the wire.

DOI: [10.1103/PhysRevB.109.045132](https://doi.org/10.1103/PhysRevB.109.045132)**I. INTRODUCTION**

A promising avenue towards achieving scalable quantum computing involves the utilization of Majorana zero modes (MZMs) [1–3], which emerge as bound states within topological superconductors [4–12]. Their occurrence is a consequence of the topological properties of the underlying phase, and they manifest as zero-energy states located within the excitation gap of the system. Due to this topological protection, MZMs exhibit robustness against external perturbations and decoherence. Furthermore, the ability to manipulate MZMs through anyonic braiding allows for the implementation of fault-tolerant qubit operations [4–7,13].

MZMs can occur in hybrid systems of conventional superconductors and semiconductors with strong spin-orbit coupling [4,14–17]. However, disorder in these systems turns out to be a major problem [18–24], as it can destroy the topological phase [25]. In addition, disorder can induce trivial Andreev bound states (ABSs) [26–44], which can mimic signatures of MZMs [18,20,41,45–48]. These ABSs complicate the verification of MZMs in experiments as they make more complex measurements and devices necessary [22,49]. To distinguish MZMs from ABSs, signatures based on coherent transport using electron interferometers [49–52] are suitable but experimentally challenging [49]. Another method to detect MZMs is the so-called topological gap protocol [53], which can be applied to a grounded wire contacted with leads at both ends. Here all elements of the conductance matrix between the two leads are measured to ensure that zero-bias conductance peaks occur simultaneously at both ends and that the excitation gap closes at the boundaries of the topological phase [53].

Numerous experimental studies have confirmed the predicted signatures of MZMs [54–65]. Promising experimental results that indicate a high likelihood for the presence of MZMs in hybrid wires have been obtained through interferometry [49] and the application of the topological gap protocol [22]. Theoretical investigations have also identified strategies for enhancing MZMs in clean Majorana wires, including the use of magnetic field textures [66–69], harmonic potential profiles [67], and optimized geometries for Majorana Josephson junctions [70]. However, the presence

of disorder in the fabrication process significantly affects the yield of Majorana devices [22], which poses a major limitation for the realization of large-scale qubit systems. Several approaches have been proposed to address this challenge. First, efforts have been made to fabricate cleaner wires by improving fabrication processes [7,71]. Additionally, it has been demonstrated that weak coupling between superconductors and semiconductors can enhance the resilience of hybrid wires to moderate disorder [72,73]. Another strategy involves utilizing machine learning optimization techniques to create a potential profile along the Majorana wire using a gate array, compensating for the effects of disorder [74]. However, the optimization process requires the measurement of coherent transport through an electron interferometer [49–52], which may pose challenges for scalability. In recent years, the increasing complexity of quantum devices [9,11,75–77] has necessitated the automatic tuning of parameters [78–89]. Machine learning algorithms have emerged as effective tools for this purpose [77,80,84,86,88,90,91]. In this paper, we propose an optimization approach that employs the CMA-ES machine learning algorithm [92] to tune the voltages on an array of gates located near a Majorana wire. Our optimization metric is based on conductance measurements, eliminating the need for interferometry. We demonstrate the effectiveness of the machine learning algorithm in finding gate voltages that minimize the metric, resulting in the reliable restoration of the topological phase, localized MZMs, and the topological gap, even in the presence of significant disorder. Notably, the optimization process effectively disregards trivial ABSs and can drive the wire from a trivial phase to a topological phase while mitigating the effects of disorder. Additionally, we discuss the convergence properties of the algorithm and argue that this optimization approach is experimentally feasible using currently available technology.

The code needed to reproduce all results is open source and has been made available online [93].

II. SETUP

We consider a grounded Majorana hybrid wire of length L that is connected to two leads (labeled L and R) at the ends

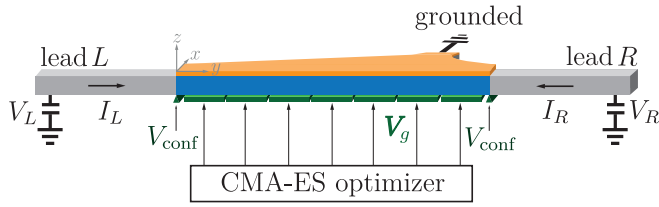


FIG. 1. Majorana hybrid wire consisting of a grounded superconductor (orange) and a semiconductor with strong spin orbit coupling (blue) connected to two leads L and R separated from the wire by a potential V_{conf} created by pinch-off gates. The full conductance matrix $G_{\alpha\beta} = dI_{\alpha}/dV_{\beta}$ can be measured as a function of an applied bias voltage $V_R - V_L$ and external Zeeman field E_z based on which voltages of an array of gates (green) are optimized using the CMA-ES algorithm [92] to cancel disorder effects in the hybrid wire.

(Fig. 1). An array of gates is placed in proximity to the wire such that the voltages on the individual gates can be controlled by the CMA-ES algorithm. Two additional gates that are not included in the optimization are used to separate the wire from the leads by creating a confinement potential.

This setup allows us to measure the entries of the conductance matrix $G_{\alpha\beta} = dI_{\alpha}/dV_{\beta}$ between the leads

$$G = \frac{e^2}{h} \begin{pmatrix} \tilde{G}_{LL} & \tilde{G}_{LR} \\ \tilde{G}_{RL} & \tilde{G}_{RR} \end{pmatrix}. \quad (1)$$

Denoting the voltage at lead α as V_{α} , the entries in units of e^2/h at zero temperature are given by [94]

$$\begin{aligned} \tilde{G}_{LL} &= N_L - R_L^e(-eV_L) + A_L^e(-eV_L) \\ \tilde{G}_{LR} &= -T_{LR}^e(-eV_R) + A_{LR}^e(-eV_R) \\ \tilde{G}_{RL} &= -T_{RL}^e(-eV_L) + A_{RL}^e(-eV_L) \\ \tilde{G}_{RR} &= N_R - R_R^e(-eV_R) + A_R^e(-eV_R). \end{aligned} \quad (2)$$

Here N_{α} is the number of channels in lead α , R_{α}^e is the reflection probability for an electron at lead α , A_{α}^e is the probability for an electron to be reflected as a hole at lead α , $T_{\alpha\alpha'}^e$ is the transmission probability for an electron from lead α to lead α' , and $A_{\alpha\alpha'}^e$ is the probability for an electron from lead α to be transmitted as a hole to lead α' [94].

Below we construct a metric for optimization based on conductance measurements. To assess whether optimization of the metric successfully restores an extended topological phase, we consider the *scattering invariant* [95],

$$\mathcal{Q} = \text{sgn det} \begin{pmatrix} r_L^{e \rightarrow e} & r_L^{e \rightarrow h} \\ r_L^{h \rightarrow e} & r_L^{h \rightarrow h} \end{pmatrix}. \quad (3)$$

This is the sign of the determinant of the reflection block obtained from the scattering matrix for lead L , containing the complex reflection amplitudes computed at zero energy. If the system is large enough such that the overlap of the MZMs is much smaller than their couplings to the lead, then the scattering invariant is $\mathcal{Q} = -1$ in the topological phase [22,95], and in the trivial phase $\mathcal{Q} = +1$ holds. However, it is important to note that this scattering invariant is not experimentally accessible and is only reported as a benchmark for assessing the performance of the optimization process for restoring the topological phase.

In addition to bringing the wire into the topological phase, a large excitation gap is targeted. We combine both properties in the so-called *topological gap* $\mathcal{Q}\Delta_{\text{gap}}$ [22], where $\Delta_{\text{gap}} = \mathcal{E}_1$ is the energy of the second level, i.e., the energy of the level above the MZM in the topological phase, which is approximately equal to the excitation gap. Therefore, a negative value for the topological gap with large magnitude is advantageous.

For our simulations, we first study an effective one-dimensional wire and consider a more realistic two-dimensional system later. The one-dimensional Majorana wire in Nambu basis $(d_{\uparrow}^{\dagger}(y), d_{\downarrow}^{\dagger}(y), d_{\downarrow}(y), -d_{\uparrow}(y))$ is modeled by the BdG Hamiltonian

$$\begin{aligned} \mathcal{H}_{\text{wire}} = \tau_z \left[-\frac{\hbar^2 \partial_y^2}{2m^*} \sigma_0 - \mu \sigma_0 - i\hbar \alpha_R \sigma_x \partial_y \right. \\ \left. + \delta_{\text{dis}}(y) \sigma_0 + V_g(y) \sigma_0 + V_{\text{conf}}(y) \sigma_0 \right] \\ - E_z \tau_0 \sigma_z + \Delta \tau_x \sigma_0, \end{aligned} \quad (4)$$

where $\hbar \alpha_R = 0.2 \text{ eV \AA}$ is the Rashba spin-orbit coupling strength and $m^* = 0.02 m_e$ is the effective mass of the electrons such that a characteristic energy scale is given by $E_{\text{so}} = \alpha_R^2 m^*/2 = 0.05 \text{ meV}$ and a characteristic length scale is $l_{\text{so}} = \hbar/(\alpha_R m^*) = 0.19 \text{ \mu m}$ —realistic values for InAs nanowires [10,54]. Here y is the direction along the wire, Δ is the proximity induced s -wave superconducting gap, μ the chemical potential, E_z the Zeeman energy due to an external magnetic field $\mathbf{B} = B e_z$, and σ_i and τ_i are Pauli matrices acting in spin and particle-hole space, respectively. We choose $\Delta = 2 E_{\text{so}}$ throughout the paper. Disorder in the wire is described by normally distributed random numbers $\delta_{\text{dis}}(y)$ with standard deviation σ_{dis} , and a finite correlation length λ_{dis} can be introduced by damping high Fourier modes (for details see Appendix A). The confinement potential V_{conf} separating the wire from the leads is given by a steep Gaussian peak at both lead-wire interfaces (see Appendix A). Only when considering tuning a wire from the ABSs regime to the topological phase, we choose a more shallow confinement.

We use the CMA-ES algorithm (for details see Appendix B), which has found many applications for high-dimensional optimization problems [96–100], to optimize the Fourier components a_i, b_i [see Eq. (5) below] of the N_g gate voltages. The Fourier components are related to the voltage V_j on gate j via

$$V_j = \frac{b_0}{2} + \sum_{k=1}^{\lfloor \frac{N_g-1}{2} \rfloor} a_k \sin\left(\frac{2\pi}{N_g} k j\right) + \sum_{k=1}^{\lfloor \frac{N_g}{2} \rfloor} b_k \cos\left(\frac{2\pi}{N_g} k j\right). \quad (5)$$

For reasons of better comparability, we set $b_0 = 0$ with the exception of the case where the optimization algorithm tunes from ABSs to MZMs. We assume that the wire is located a distance $z_{\text{sys}} = 0.3 E_{\text{so}}$ above the gates such that the potential created by the gate array at position y in the wire is given by

$$V_g(y) = \mathcal{F}^{-1} \left[e^{-|q|z_{\text{sys}}} \mathcal{F} \left[\sum_{j=1}^{N_g} V_j \chi_j(y) \right] \right]. \quad (6)$$

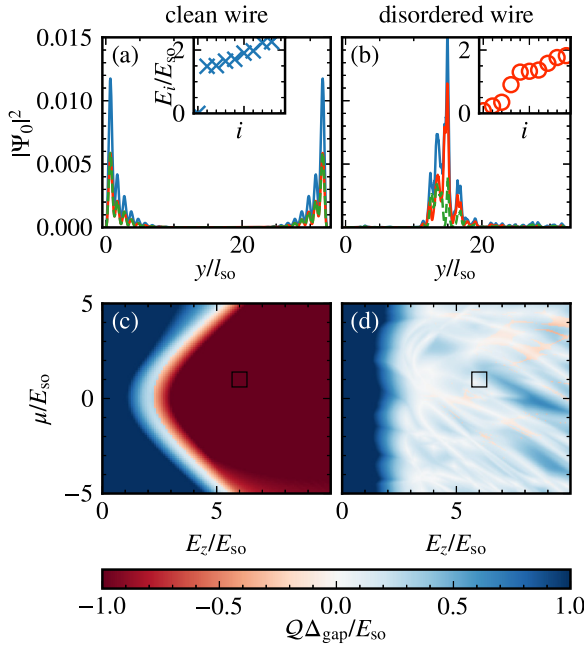


FIG. 2. Effects of strong disorder on a Majorana wire of length $L = 32.5 l_{so}$ in the topological phase for $\mu = 1 E_{so}$ and $E_z = 6 E_{so}$. Panels (a) and (b) depict the wave functions $|\Psi_0|^2$ (blue) of the lowest energy state together with the electron $|u_0|^2$ (green) and hole wave function $|v_0|^2$ (orange) for a clean and disordered wire ($\sigma_{dis} = 25 E_{so}$, $\lambda_{dis} = 0$), respectively. Here $\Psi_0 = (u_0, v_0)$ such that $|\Psi_0|^2 = |u_0|^2 + |v_0|^2$. The insets depict the lowest energy levels. Panels (c) and (d) show the corresponding topological gaps $Q\Delta_{gap}$, where Q is the scattering invariant and Δ_{gap} is an estimator for the gap given by the energy of the second level. The black squares indicate the parameters used in panels (a) and (b), respectively. While the clean wire shows localized Majorana zero modes with a large topological gap ($Q = -1$, $\Delta_{gap} > 1 E_{so}$), both the localized zero modes and the topological phase are destroyed by strong disorder.

Here \mathcal{F} and \mathcal{F}^{-1} denote Fourier transform and inverse Fourier transform, respectively, and $\chi_j(y)$ is one for y above gate j and zero otherwise.

For computing the conductance, the eigenstates, and the energy eigenvalues of the Hamiltonian Eq. (4), we discretize the Hamiltonian on a lattice with spacing $a = 0.026 l_{so}$, and use the python package KWANT [101] to extract the scattering matrix, the conductance matrix, and the Hamiltonian matrix. As a point of reference, we consider a clean wire in Fig. 2, for which the topological gap shows an extended topological phase as a function of Zeeman field and chemical potential for $E_z^2 > \mu^2 + \Delta^2$ [red region in Fig. 2(c)] with a gap closing at the boundary [white region in Fig. 2(c)]. In the topological phase, there exists a zero energy state in the gap [inset of Fig. 2(a)] with a wave function localized at the wire ends [Fig. 2(a)]. For this Majorana wave function $\Psi_0 = (\mathbf{u}_0, \mathbf{v}_0)$, the Majorana condition $|\mathbf{v}_0(y)| = |\mathbf{u}_0(y)|$ holds between electron [$\mathbf{u}_0 = (u_\uparrow, u_\downarrow)$ in green] and hole components (\mathbf{v}_0 in orange). However, when adding strong onsite disorder (see Appendix C) with standard deviation $\sigma_{dis} = 25 E_{so}$, the topological phase and the gap are destroyed [Fig. 2(d)]. The eigenstate with the smallest energy is no longer localized at the wire ends and does not fulfill the Majorana condition

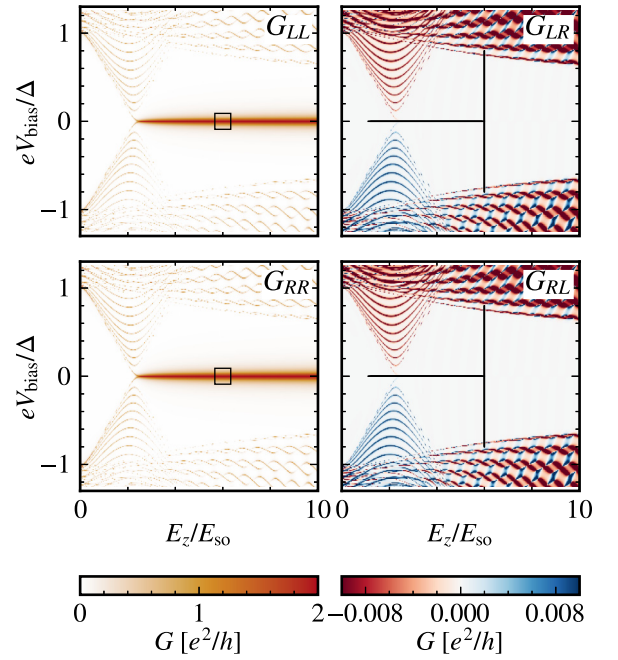


FIG. 3. Elements of the conductance matrix between lead L and R as a function of the Zeeman field E_z and bias voltage V_{bias} at a chemical potential $\mu = 1 E_{so}$ in a clean wire of length $L = 32.5 l_{so}$. For evaluating the metric, a measurement of G_{RR} and G_{LL} at zero bias is performed (black square), and a scan of the nonlocal conductances along E_z for zero bias and along V_{bias} for a given E_z are needed (black lines). Increasing the Zeeman field E_z , the wire enters the topological phase which shows zero bias peaks in the local conductance at both leads. At the transition, the gap closes which can be inferred from the nonlocal conductance.

anymore. To compensate the effects of such disorder, in the following, we first introduce a metric and then minimize it by letting the CMA-ES algorithm find optimal gate voltages. As we will demonstrate, this optimization is capable of restoring the topological phase and the Majorana zero mode.

III. METRIC BASED ON CONDUCTANCE MEASUREMENTS

It is crucial for a successful optimization to choose a metric that enhances the desired features when minimized. As disorder can induce trivial ABSs at zero energy, the metric cannot solely rely on the occurrence of zero-bias conductance peaks. We suggest the following metric:

$$\mathcal{M}(\mathbf{V}_g; E_z, \mu) = -\tilde{G}_{LL}(V_b = 0)\tilde{G}_{RR}(V_b = 0) \frac{2\hat{\Delta}_{gap}}{\Delta} \times \left| \ln \max_{E \in E_z} \sum_{\alpha} \tilde{G}_{\alpha\alpha}(E_z = E) \right|^{-1}, \quad (7)$$

where the sum runs over the lead index $\alpha = L, R$. This metric consists of the following contributions inspired by the topological gap protocol [53], as illustrated for the clean wire in Fig. 3:

(1) As a first contribution the local zero-bias conductance $\tilde{G}_{\alpha\alpha}(V_b = 0) \equiv (h/e^2) G_{\alpha\alpha}(\mathbf{V}_g, V_b = 0; E_z, \mu)$ at both leads is

measured (left panels). Their product is large if there are zero-bias peaks at both ends, as is the case for localized MZMs.

(2) As a second contribution, to ensure that the zero-bias peaks are not realized by simply closing the gap, we include an estimator for the transport gap $\hat{\Delta}_{\text{gap}}(\mathbf{V}_g; E_z, \mu)$ obtained from a scan of the antisymmetric part of the nonlocal conductance $G_{\alpha\bar{\alpha}}^{\text{asym}} = [G_{\alpha\bar{\alpha}}(eV_b) - G_{\alpha\bar{\alpha}}(-eV_b)]/2$ over a range of bias voltages $V_b = V_R - V_L$ (black, vertical lines in right panels). This scan is performed by increasing the bias using a step size $\delta V_b = 0.05 E_{\text{so}}$ until the signal peaks at $eV_b = \hat{\Delta}_{\text{gap}}$, indicating extended state above the gap. The rescale factor $2/\Delta$ balances the metric such that if the transport gap is the full proximity gap Δ , the contribution to the metric is 2—the same factor each zero-bias peak would contribute in (1) for ideal MZMs.

(3) The third contribution involves a scan of the nonlocal conductances $\tilde{G}_{\alpha\bar{\alpha}}(\mathbf{V}_g, V_b = 0; E_z, \mu)$ over Zeeman fields in the interval $I_{E_z} = [E_z - 5 E_{\text{so}}, E_z]$ (black, horizontal lines in right panels) with step size $\delta E_z = 0.15 E_{\text{so}}$, where $\bar{\alpha}$ is the opposite lead of α . The contribution to the metric is then given by the logarithm of the maximum of the sum of these nonlocal conductances, where taking the logarithm ensures that the metric is not dominated by this term as the nonlocal conductance can change by several orders of magnitude during optimization. This term is large if there is a gap closing at a Zeeman field in the interval, which is the case if the transition to the topological phase occurs for a Zeeman field smaller than E_z .

This metric does not require performing the full gap protocol, which would be too slow if many metric measurements are needed, but a metric evaluation only requires two parameter scans, one along the bias voltage for fixed Zeeman field and one along the Zeeman field for fixed bias.

IV. OPTIMIZATION OF A ONE-DIMENSIONAL MAJORANA WIRE

We next revisit the Majorana wire of length $L = 32.5 l_{\text{so}}$ with strong onsite disorder $\sigma_{\text{dis}} = 25 E_{\text{so}}$ considered in the right panels of Fig. 2. For a Zeeman energy of $E_z = 6 E_{\text{so}}$ and a chemical potential of $\mu = 1 E_{\text{so}}$, we use the CMA-ES algorithm to optimize voltages of $N_g = 50$ gates to minimize the metric Eq. (7) (for optimization with fewer gates see Appendix D). The CMA-ES algorithm is a derivative-free, population-based machine learning algorithm [92]: In each step of the optimization a population, i.e., a set of n_{pop} candidate gate voltage configurations, is drawn from a multivariate normal distribution. Then the metric is measured for each candidate in the population. The only information about the physical system that the algorithm needs is the value of the metric for each candidate, and based on the $n_{\text{pop}}/2$ best candidates, the parameters of the algorithm that determine the search region are updated. The idea is that the search region from which the population is drawn can first expand to find candidates close to the minimum and then contract around the minimum. For a detailed description of the CMA-ES algorithm, we refer the reader to Ref. [92] and Appendix B, and details on applying the algorithm to gate array optimization can be found in Ref. [74].

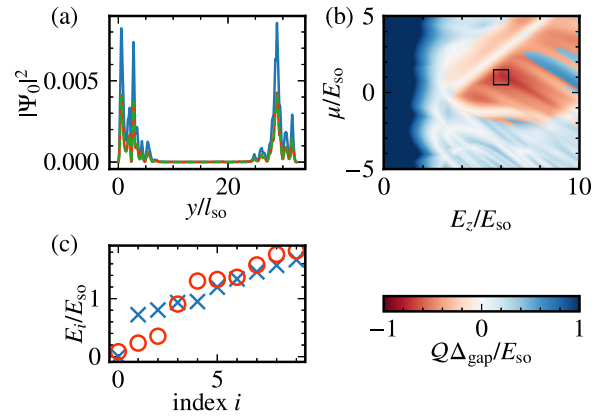


FIG. 4. Majorana wire with strong disorder [cf. Fig. 2(b)] using optimized gate voltages found by minimizing the metric Eq. (7) with the CMA-ES algorithm. (a) Wave function $|\Psi_0|^2$ (blue) of the first level together with the electron $|u_0|^2$ (green) and hole wave function $|v_0|^2$ (orange), (b) topological gap $Q\Delta_{\text{gap}}$, and (c) the energy levels for the optimized wire (blue) and for comparison for the disordered wire with zero voltage on all gates (red). Using optimized gate voltages restores localized MZMs, the topological phase, and a topological gap.

Figure 4 depicts the Majorana wave function, energy levels, and topological gap when using the optimized gate voltages found by the CMA-ES algorithm. The algorithm is capable of restoring localized MZMs such that the Majorana condition holds again [Fig. 4(a)]. A scan of the topological gap through chemical potentials μ and Zeeman energies E_z [Fig. 4(b)] reveals that optimization not only restores the topological phase at the point of optimization ($\mu = 1 E_{\text{so}}$, $E_z = 6 E_{\text{so}}$) but for an extended region (shown in red in Fig. 4(b)). In addition, the gap is restored, as can be seen from the comparison of the energy levels before optimization [Fig. 4(c), red circles] and for the optimized voltages [Fig. 4(c), blue crosses]. These results indicate that the algorithm is indeed able to learn the disorder profile as it found gate voltages such that the potential profile created along the wire compensates the disorder (see also Appendix E on the stability of the optimum).

We further show that the optimized wire lies in an extended region with zero-bias conductance peaks at both ends (Fig. 5, left panels), where the nonlocal conductances (Fig. 5, right panels) indicate that the boundary of this region is gapless, while there is a finite gap within the region.

V. COMPARISON BETWEEN THE METRIC AND THE TOPOLOGICAL GAP

Since the desired properties of the system—the topological phase and a large excitation gap—are encoded in the topological gap $Q\Delta_{\text{gap}}$, one may assume that it is an ideal metric for optimization. Unfortunately, however, the scattering invariant cannot be accessed experimentally, which disqualifies it for this purpose. To further motivate our metric, Eq. (7), we show a comparison with the topological gap in Fig. 6. For this, we calculate both quantities as a function of chemical potential μ and Zeeman energy E_z for the clean wire (top panels), the

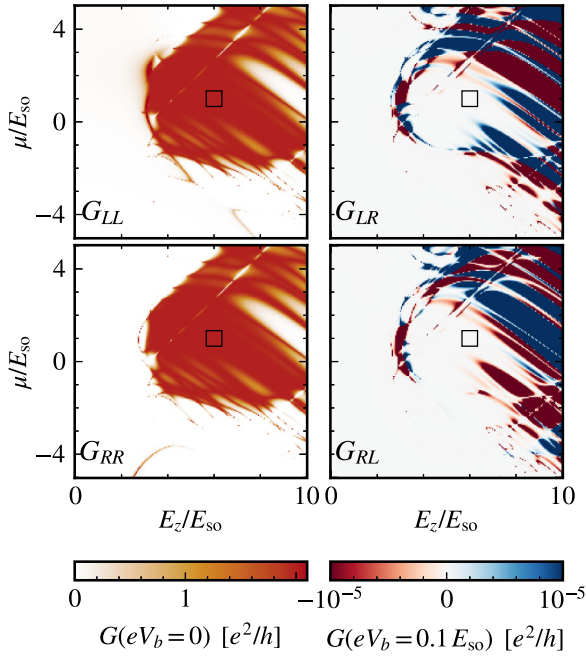


FIG. 5. Elements of the conductance matrix between lead L and R as a function of the Zeeman field E_z and chemical potential μ for the disordered wire with optimized gate voltages (see Fig. 4). The local conductances are shown at zero bias and the nonlocal conductances for a small bias voltage of $V_{\text{bias}} = 0.1 E_{\text{so}}$. These conductance measurements indicate an extended topological phase with gap closing along the boundary [53]. The black square indicates the point in the phase diagram at which the optimization has been performed.

disordered wire with $\sigma_{\text{dis}} = 25 E_{\text{so}}$, $\lambda_{\text{dis}} = 0$ (center panels), and the disordered wire with optimized gate voltages (bottom panels). We find excellent agreement between our metric and the topological gap. It turns out that minimizing the metric leads to a topological phase with sizable excitation gap, and the absence of *false positives* makes the optimization reliable for recovering the topological phase (see also Appendix F for more disorder realizations).

VI. CONVERGENCE OF THE OPTIMIZATION

Full convergence of the algorithm, such that for the best gate configurations at step t and $t - 1$ holds that $\|\mathbf{V}_g^{(t)} - \mathbf{V}_g^{(t-1)}\| < 10^{-8} E_{\text{so}}$, may require tens of thousands of calculations (or measurements) of the metric, which would be experimentally very time-consuming. However, our aim is not to achieve full convergence, but to reliably compensate the disorder effects. We therefore consider Majorana wave functions, energy levels, and the topological gap at several steps during the optimization in Fig. 7. The starting point for the optimization is again the disordered wire in the right panel of Fig. 2 with zero voltage on all gates. It becomes apparent that the magnitude of the metric increases rapidly during the initial steps and that the slope subsequently flattens out (upper left panel). After only 40 metric measurements, localized MZMs are recovered at the point (μ, E_z) . Already after 2680 metric measurements, an extended topological phase with

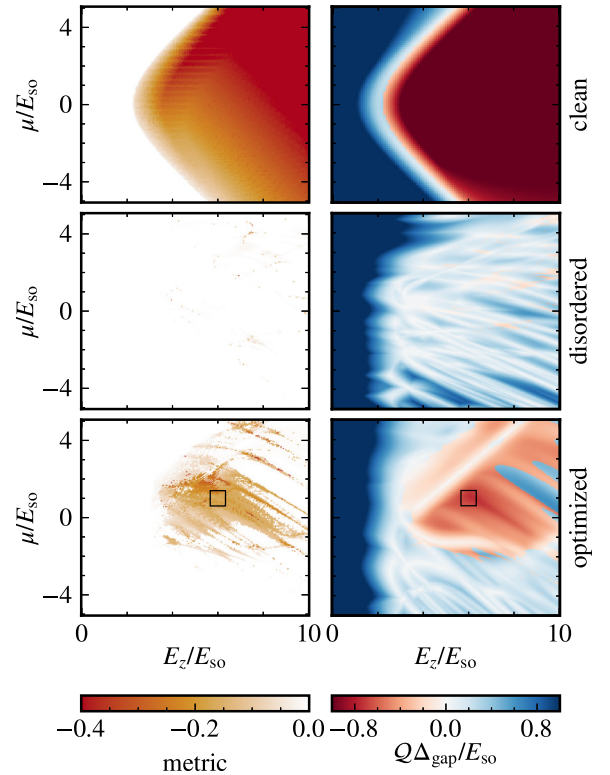


FIG. 6. Comparison between the measurable metric (left panels) and the experimentally inaccessible topological gap $Q\Delta_{\text{gap}}$ (right panels) as a function of Zeeman energy E_z and chemical potential μ . The top panels depict a clean wire, the center panels a wire with strong disorder and zero voltage on all gates, and the lower panels show a wire with strong disorder and optimized gate voltages. The metric is small where the topological gap indicates a strong topological phase ($Q = -1$ and large gap), and the topological phase can be accurately inferred from the values of the metric.

considerable gap is obtained, and after 3280 measurements we no longer observe any significant improvements in the topological gap anymore, although the metric continues to increase slightly. From these observations, we conclude that complete recovery of the MZMs occurs significantly before formal convergence, so that a feasible number of much less than 5000 evaluations of the metric is sufficient. In Appendix F, we show further optimizations for various disorder realizations after 3000 metric evaluations and find similar results. In our simulations, one metric evaluation requires in total less than 100 conductance measurements for the scans along Zeeman field and bias voltage.

VII. OPTIMIZATION IN THE PRESENCE OF ANDREEV BOUND STATES

The problem of a single conductance measurement is that it cannot distinguish between trivial ABSs pinned at zero energy and topological MZMs. This raises the question whether optimization of the metric, Eq. (7), is able to ignore ABSs and tune the wire into the topological phase while simultaneously compensating for disorder.

By choosing a smooth confinement potential that slowly decays into the inside of the wire (see Appendix A for details),

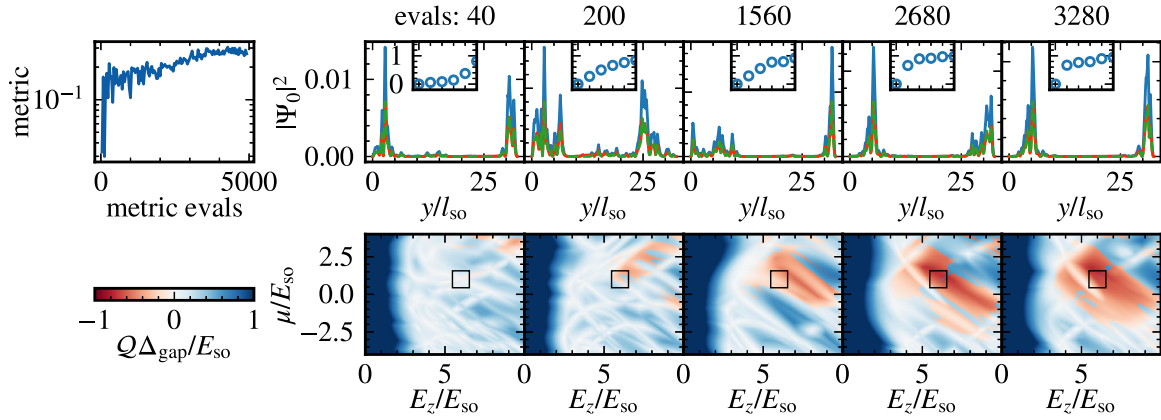


FIG. 7. Convergence of the optimization algorithm for a wire of length $L = 32.5 l_{\text{so}}$ with strong onsite disorder with a strength of $\sigma_{\text{dis}} = 25 E_{\text{so}}$. The upper left-hand panel depicts the magnitude of the metric as a function of the number of metric evaluations. The other upper panels show the wave functions and the insets the lowest energy levels during several steps of the optimization before the algorithm has fully converged, and the lower panels show the corresponding topological gaps. To restore the localization of Majorana modes, only a few hundred metric evaluations are needed, and for obtaining an extended topological phase, a few thousand metric evaluations are sufficient even before full convergence of the CMA-ES algorithm.

extended regions with a pair of ABSs at zero energy appear in the trivial phase [26] (white region in top panel of Fig. 8), each localized at one end of the wire, thus giving rise to zero-bias conductance peaks at both ends [26].

As a starting point for optimization, we choose a chemical potential of $\mu = 8 E_{\text{so}}$ and Zeeman energy $E_z = 6 E_{\text{so}}$, which corresponds to the trivial phase with ABSs. In addition, we introduced strong disorder $\sigma_{\text{dis}} = 50 E_{\text{so}}$ with very short correlation length $\lambda_{\text{dis}} = 0.052 l_{\text{so}}$, which causes the topological phase to vanish and destroys the localization of trivial ABSs (center panel in Fig. 8). To allow the algorithm to tune out of the trivial phase into the topological phase, we here include the mean gate voltage b_0 in Eq. (5) in the optimization. We find that the CMA-ES algorithm successfully compensates for the disorder while also ignoring the ABSs and tuning the wire into the topological phase (lower panel), resulting in localized MZMs.

VIII. OPTIMIZATION OF A TWO-DIMENSIONAL MAJORANA WIRE

We next focus on a two-dimensional, rectangular wire of length $L_y = 19.5 l_{\text{so}}$ and width $L_x = 0.39 l_{\text{so}}$ described by the Hamiltonian

$$\begin{aligned} \mathcal{H}_{\text{wire}}^{2d} = \tau_z \left[-\frac{\hbar^2}{2m^*} (\partial_x^2 + \partial_y^2) \sigma_0 - \mu \sigma_0 + \delta_{\text{dis}}(x, y) \sigma_0 \right. \\ \left. - i\hbar \alpha_R (\sigma_x \partial_y - \sigma_y \partial_x) + V_g(x, y) \sigma_0 \right. \\ \left. + V_{\text{conf}}(y) \sigma_0 \right] + \frac{\mu_B g B_z}{2} \tau_0 \sigma_z + \Delta \tau_x \sigma_0. \end{aligned} \quad (8)$$

Here the Landé factor is given by $g = -14.9$ [102], and if not stated otherwise, the same parameters as for the one-dimensional wire are chosen. When discretizing the Hamiltonian on a two-dimensional lattice with spacings $a_x = a_y = 0.026 l_{\text{so}}$, we include the orbital effect of the magnetic field by adding Peierls phases $e^{-ie/\hbar \int_{r_1}^{r_2} \mathbf{A} \cdot d\mathbf{r}}$ to the hoppings

from site \mathbf{r}_1 to \mathbf{r}_2 . We choose the vector potential \mathbf{A} such that it is given by $-B_z x \mathbf{e}_y$ away from the ends and smoothly vanishes over a distance $L_x/2$ towards the short ends of the wire in order to conserve the supercurrent in the wire [74].

The clean two-dimensional wire is in the first topological phase for a chemical potential of $\mu = 63 E_{\text{so}}$ and a Zeeman energy $E_z = \mu_B g B_z / 2 = 6 E_{\text{so}}$, which we choose as parameters for the optimization. Adding strong disorder with strength $\sigma_{\text{dis}} = 120 E_{\text{so}}$ and a short correlation length $\lambda_{\text{dis}} = 0.052 l_{\text{so}}$ completely destroys MZMs (Fig. 9, upper left panel) and the topological phase (lower left panel) similarly to the one-dimensional case. Again optimization of $N_g = 50$ gates allows restoring localized MZMs (upper right panel) and an extended topological phase (lower right panel).

IX. CONCLUSIONS

In this study, we explored the machine learning optimization of a gate array placed in proximity to a strongly disordered Majorana wire. To optimize the system using the CMA-ES algorithm, we introduced a metric based on conductance measurements. This metric allowed for the optimization of a grounded wire connected to two leads, eliminating the need for interferometry and Coulomb blockade. By minimizing the metric, the CMA-ES algorithm effectively restored the localized MZMs, extended the topological phase, and reopened the excitation gap, even in cases where they were completely destroyed by the disorder. Remarkably, the algorithm demonstrated the capability to disregard trivial ABSs and to tune the wire into the topological phase while simultaneously mitigating the effects of disorder. Furthermore, we demonstrated that the required number of measurements for the optimization process is experimentally feasible, and even with a modest number of gates (around 20–50), substantial improvements can be achieved. Notably, gate arrays of this scale can already be constructed using standard electron beam lithography and aluminum gates isolated by native oxide [82,103].

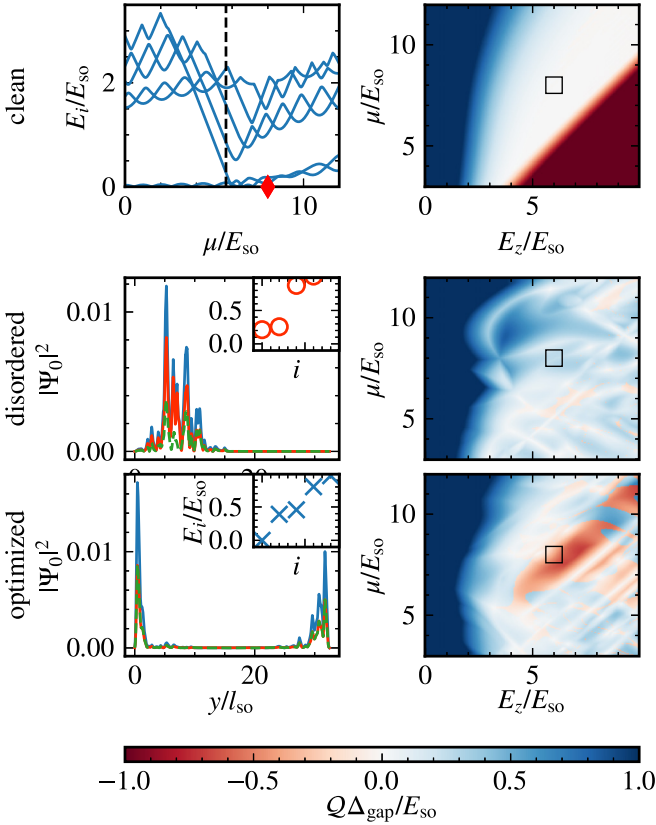


FIG. 8. Results for a wire with a smooth confinement potential that supports ABSs in the trivial phase. The upper panels show the lowest energy levels as a function of the chemical potential (left) and the topological gap (right) as a function of Zeeman field and chemical potential for a clean wire as a reference. Optimization is started in the trivial phase (red diamond), where a pair of ABSs is present in a clean wire when all gate voltages are set to zero. The center panels depict the wave function of the first level $|\Psi_0|^2$ (blue, left panel) with their decomposition into hole (orange) and electron (green) components and the topological gap for the case of strong disorder $\sigma_{\text{dis}} = 50 E_{\text{so}}$, $\lambda_{\text{dis}} = 0.052 l_{\text{so}}$, where all gate voltages are zero. The bottom panels show wave function and topological gap for using optimized gate voltages, where the mean voltage b_0 is included in the optimization. The insets in the wave function panels show the corresponding lowest energy levels. Optimizing the metric tunes the system to the topological phase—ignoring the trivial ABSs.

Recently, simultaneous tuning of the spatial profiles of the induced superconducting pairing, Zeeman field, and spin-orbit coupling have been proposed to produce false-positives of the topological gap protocol [104]. While there is an ongoing discussion about how realistic such situations are [105,106], and whether they can really fool the gap protocol [107], they may result in a large metric when optimizing Majorana wires. However, these spatial profiles cannot be actively produced by the gate arrays of our method, such that the optimization will not steer the system into such a situation over restoring the topological phase.

Tuning scalable architectures remains a major challenge, primarily due to the demand for controlling many individually tunable gates. Nonetheless, the automated tuning of individual wires and smaller systems allows for proof-of-principle

experiments, fostering a deeper understanding of disorder mitigation. In addition, material improvements resulting in less disorder may reduce the requirements in the number of gates and thus improve scalability. The analysis of optimally tuned gate voltage arrays may also offer guidance in optimizing the design of Majorana wires.

ACKNOWLEDGMENTS

This work has been funded by the Deutsche Forschungsgemeinschaft (DFG) under Grants No. RO 2247/11-1 and No. 406116891 within the Research Training Group RTG 2522/1.

APPENDIX A: DETAILS ON DISORDER AND CONFINEMENT POTENTIALS

To obtain correlated disorder potentials, we first draw random numbers δ with standard deviation σ_{dis} from a normal distribution. A finite correlation length λ_{dis} can be included by damping high Fourier modes according to [74]

$$\delta_{\text{dis}}(y) = \mathcal{F}^{-1}[e^{-|q|\lambda_{\text{dis}}}\mathcal{F}[\delta(y)]]]. \quad (\text{A1})$$

For most of the one-dimensional wires considered here, we choose onsite disorder $\lambda_{\text{dis}} = 0$, which is the most challenging type of disorder to compensate using gate potentials [74]. For the two-dimensional wire, we consider the case $\lambda_{\text{dis}} = 0.052 l_{\text{so}}$, which is a very short correlation length.

A confinement potential V_{conf} separates the wire from the leads where we lower the potential by $V_{\text{lead}} = 100 E_{\text{so}}$ to ensure that both spin species are present at the Fermi level in the leads. Except for Sec. VII, we consider a steep confinement of the form $V_{\text{conf}}(y) = V_{\sigma,V_0}(y - y_0) + V_{\sigma,V_0}(y - L + y_0)$ with $V_{\sigma,V_0}(y) = V_0 \exp[-y^2/2\sigma^2]$, $\sigma = 0.1 E_{\text{so}}$, and $V_0 = 65 E_{\text{so}}$. Here $y_0 = \sqrt{2\sigma^2 \ln 2}$ such that the potential maximum is moved a distance y_0 into the wire and the potential has decayed to $V_0/2$ at the wire lead interface.

In Sec. VII, we use a smooth confinement potential in order to produce a region of ABSs at zero energy in the trivial phase [26,108]. The potential is made up of a narrow Gaussian peak with decay length $\sigma_1 = 0.1 l_{\text{so}}$ and a wide peak with $\sigma_2 = 6 l_{\text{so}}$ continuously matched at $(y_1 + y_0, E_s)$. At the left lead, the potential is given by

$$V(y) = \begin{cases} V_{\sigma_1, V_0 + V_{\text{lead}}}(y - y_0) - V_{\text{lead}} & y \leq 0 \\ V_{\sigma_1, V_0}(y - y_0) & 0 < y < y_1 \\ V_{\sigma_2, V_0}(y - y_0 - y_1 + y_2) & y \geq y_1 \end{cases}$$

$$y_0 = \sqrt{2\sigma^2 \ln 2}, \quad (\text{A2})$$

$$y_j = \sqrt{2\sigma_j^2 \ln(V_0/E_s)}. \quad (\text{A3})$$

We choose $E_s = 10 E_{\text{so}}$, $V_0 = 65 E_{\text{so}}$, and $V_{\text{lead}} = 100 E_{\text{so}}$.

APPENDIX B: DETAILS ON CMA-ES OPTIMIZATION

In each step t of the CMA-ES algorithm [92], we draw a population of $n_{\text{pop}} = 40$ gate voltage configurations—or rather their Fourier components (\mathbf{a}, \mathbf{b}) —from a multivariate normal distribution $\mathcal{N}((\mathbf{a}^{(t)}, \mathbf{b}^{(t)}), (\sigma^{(t)})^2 \mathbf{C}^{(t)})$. Here $(\mathbf{a}^{(t)}, \mathbf{b}^{(t)})$ is the mean of step t obtained as a weighted average of the $n_{\text{pop}}/2$ best candidates of step $t - 1$, i.e., the candidates with

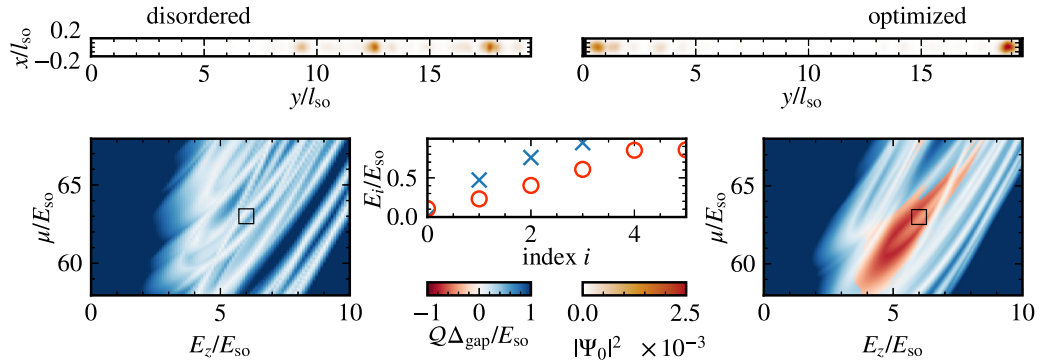


FIG. 9. Optimization of a two-dimensional wire with strong disorder of strength $\sigma_{\text{dis}} = 120 E_{\text{so}}$ and short correlation length $\lambda_{\text{dis}} = 0.052 l_{\text{so}}$ in the first topological phase for $\mu = 63 E_{\text{so}}$ and $E_z = 6 E_{\text{so}}$. The upper panels show the wave functions $|\Psi_0|^2$ for the disordered wire with zero voltage on all gates (left) and for optimized gate voltages (right). The corresponding topological gaps $Q\Delta_{\text{gap}}$ are shown in the panels below. The lower center panel shows the lowest energy levels of the wire before optimization (red circles) and with optimized voltages (blue crosses). While the disorder completely destroys the localization of the wave function of the first level and the topological gap, both are restored when using optimized gate voltages.

the smallest value for the metric. The other parameters are the step size $\sigma^{(t)}$ and the correlation matrix $\mathbf{C}^{(t)}$ adjusted by the CMA-ES algorithm to find candidates close to the minimum and contract the search region around it [92]. As initial

parameters, we set $\sigma^{(0)} = 1.0$, $\mathbf{C}^{(0)} = \mathbb{1}$, and $(\mathbf{a}^{(0)}, \mathbf{b}^{(0)}) = 0$, i.e., zero voltage on all gates. We use the mature python implementation `pycma` [109] with formal convergence criteria $\text{topfun} = 10^{-15}$, $\text{tolfunhist} = 10^{-8}$, and $\text{tolx} = 10^{-5} E_{\text{so}}$ and otherwise default parameters to perform the CMA-ES optimization computations.

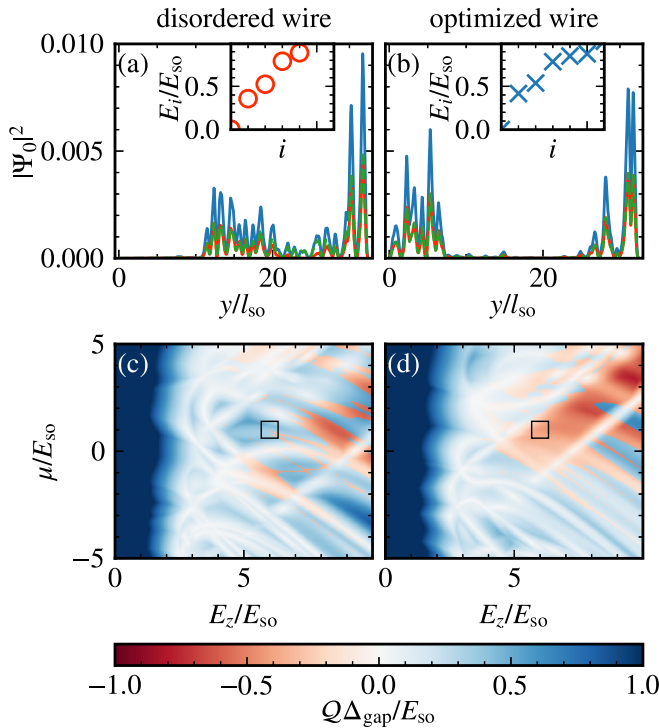


FIG. 10. Optimization of only 20 gates in proximity to a Majorana wire of length $L = 32.5 l_{\text{so}}$ with chemical potential $\mu = 1 E_{\text{so}}$ and Zeeman energy $E_z = 6 E_{\text{so}}$. Panels (a) and (b) depict the wave functions $|\Psi_0|^2$ (blue) of the first level together with the electron $|u_0|^2$ (green) and hole wave function $|v_0|^2$ (orange) for the disordered wire with short correlations ($\sigma_{\text{dis}} = 25 E_{\text{so}}$, $\lambda_{\text{dis}} = 0.05 l_{\text{so}}$) and for the same wire with optimized gates, respectively. Panels (c) and (d) show the corresponding topological gaps $Q\Delta_{\text{gap}}$. Optimization of only 20 gates restores an extended topological phase and the localization of the MZMs.

APPENDIX C: STRENGTH OF DISORDER

In this Appendix, we relate the disorder strength σ_{dis} to the mean free path ℓ and the mobility μ_e of the electrons in the wire. For a one-dimensional wire, using Fermi's golden rule and assuming there is one scatterer per lattice site, the

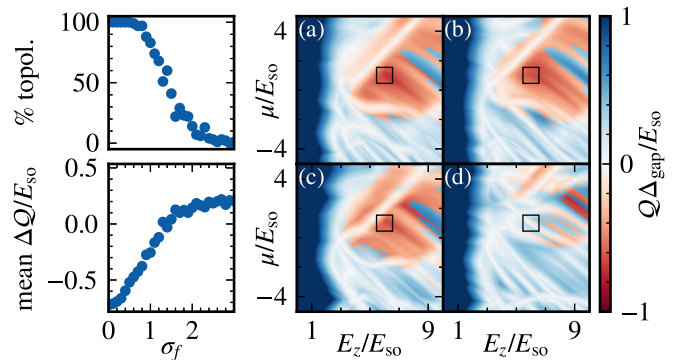


FIG. 11. Robustness of the restored topological phase of the results presented in Fig. 4 to perturbations of the optimized Fourier components. The top left panel depicts the percentage of cases with perturbed Fourier components for which the wire is topological as a function of the perturbation strength σ_f based on 100 realizations of the perturbation for each value of σ_f . The bottom left panel shows the mean of the topological gap as a function of σ_f . The right panels depict topological gap scans through the space of chemical potentials and Zeeman fields at the four perturbation strengths (a) $\sigma_f = 0.1$, (b) $\sigma_f = 0.4$, (c) $\sigma_f = 0.6$, and (d) $\sigma_f = 1.5$.

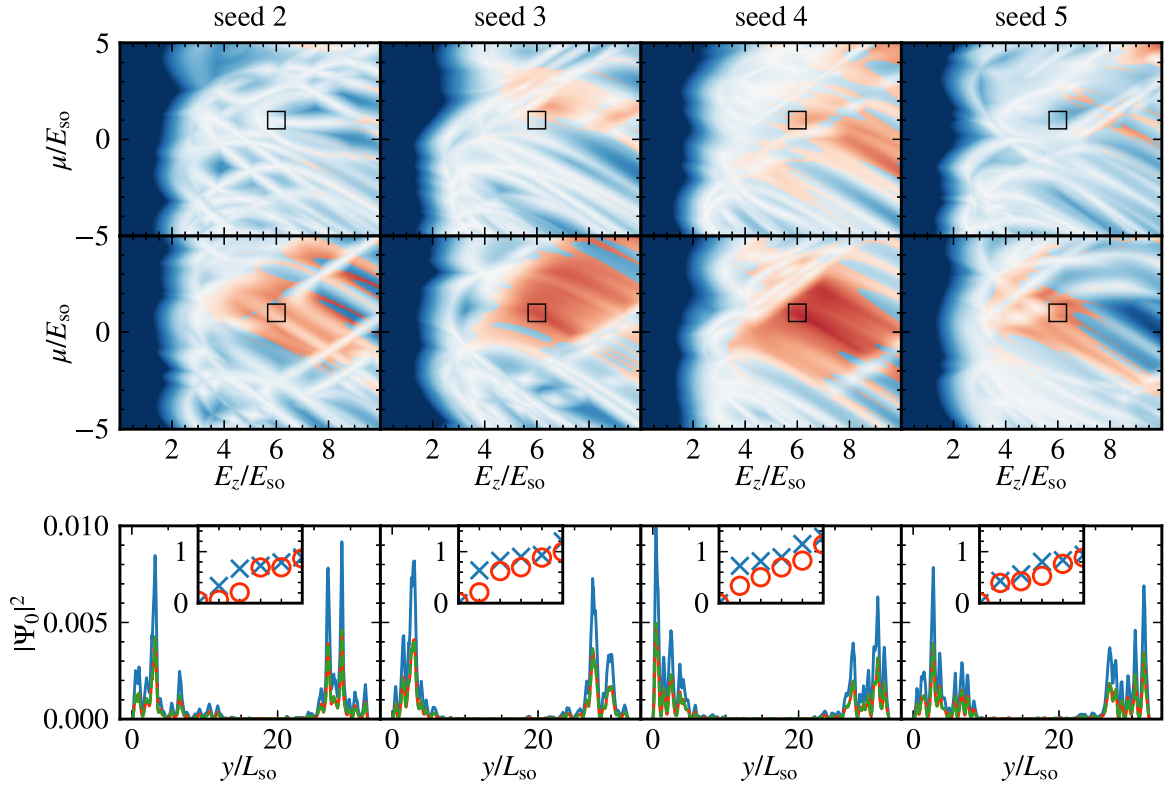


FIG. 12. Optimization results for a one-dimensional wire of length $L = 32.5 l_{so}$ with different realizations of the onsite disorder with strength $\sigma_{dis} = 25 E_{so}$ (by using different seeds of the random number generator for drawing disorder profiles; cf. Fig. 4 for seed 1). Top panels depict the topological gap $Q\Delta_{gap}$ before optimization with zero voltage on all gates. The center panels show the topological gap for optimized gate voltages after 3000 metric evaluations (75 CMA-ES steps with population size 40). The lower panels show the corresponding wave functions after optimization $|\Psi_0|^2$ (blue), the electron component $|u_0|^2$ (green), and the hole component $|v_0|^2$ (orange). The insets depict the lowest energy levels before optimization (red circles) and after optimization (blue crosses). Optimization yields an extended topological phase for all considered disorder realizations.

scattering rate is given by

$$\frac{\hbar}{\tau_{1d} E_{so}} \approx \left(\frac{\sigma_{dis}}{E_{so}} \right)^2 \frac{a}{l_{so}} \frac{1}{k_F l_{so}}. \quad (C1)$$

Here a is the lattice constant and k_F the Fermi momentum. From the scattering rate, the mean free path can be obtained as $\ell = v_F \tau_{1d}$, where v_F is the Fermi velocity. The mobility is given by $\mu_e = e\tau_{1d}/m^*$ with the effective electron mass m^* . The disorder considered here, where $\sigma_{dis} = 25 E_{so}$ for chemical potential $\mu = 1 E_{so}$ and Zeeman energy $E_z = 6 E_{so}$, corresponds to a mean free path of $\ell \approx 173$ nm and a mobility of $\mu_e \approx 22.1 \times 10^4$ cm²/Vs.

The disorder is *strong* if the scattering rate from the impurities is on the order of the induced effective gap

$$\Delta_{p,ind} = \Delta \frac{2k_F l_{so}}{\sqrt{(E_z/E_{so})^2 + 4(k_F l_{so})^2}} \quad (C2)$$

in the wire [110–116]. The disorder strength at which $\hbar/\tau_{1d} = \Delta_{p,ind}$ is given by [52]

$$\frac{\tilde{\sigma}_{dis}}{E_{so}} = \sqrt{2 \frac{l_{so}}{a} \frac{\Delta}{E_{so}} \frac{k_F l_{so}}{[(E_z/E_{so})^2 + 4(K_F l_{so})^2]^{1/4}}}. \quad (C3)$$

For $E_z = 6 E_{so}$ and $\mu = 1 E_{so}$, we find $k_F \approx 3.1 l_{so}^{-1}$ and $\tilde{\sigma}_{dis} \approx 4.5 E_{so}$, which is about five times smaller than the disorder strength considered here.

For the two-dimensional wire, the scattering rate is given by

$$\frac{\hbar}{\tau_{2d} E_{so}} \approx \frac{1}{2} \left(\frac{\sigma_{dis}}{E_{so}} \right)^2 \left(\frac{a}{l_{so}} \right)^2. \quad (C4)$$

Comparing to the one-dimensional case, Eq. (C1) reveals that the scattering rates differ by a factor $(k_F l_{so})^{-1}/(a/2l_{so}) \approx 24.6$, i.e., the mobility and mean free path are about 24.6 times larger in the two-dimensional case when using the same disorder strength σ_{dis} . We compensate for this fact by choosing $\sigma_{dis} = 120 E_{so}$ for the two-dimensional and $\sigma_{dis} = 25 E_{so}$ for the one-dimensional wire, such that $120^2/25^2 \approx 23$ makes up for this difference. By this choice, the disorder effects are of similar strength in both cases.

APPENDIX D: OPTIMIZATION WITH A REDUCED NUMBER OF GATES

In Ref. [74] a sweet spot in the number of gates for optimization of Majorana wires was identified as about 1.5–2 gates per $1 l_{so}$ of wire length. For the wires of length $L = 32.5 l_{so}$ considered here, using 50 gates is within this range. However, the larger the number of gates, the more challenging is the implementation for larger scale devices. We therefore also consider optimization using only 20 gates. In Fig. 10, we show optimization for strong disorder $\sigma_{dis} = 25 E_{so}$ with

short correlation length $\lambda_{\text{dis}} = 0.05 l_{\text{so}}$ —much smaller than the extension of an individual gate ($1.625 l_{\text{so}}$). While disorder destroys the localization of the MZMs and most of the topological phase [Figs. 10(a) and 10(c)], optimization of 20 gates is capable of restoring an extended topological phase and the MZM localization [Figs. 10(b) and 10(d)]. These results indicate that a much smaller number of gates than the sweet spot is already sufficient to improve Majorana devices. In case of larger correlation lengths or smaller disorder strength, we expect that optimizing an even smaller number of gates yields significant improvements for the performance of Majorana devices.

APPENDIX E: STABILITY OF RESTORED TOPOLOGICAL PHASE AGAINST PERTURBATIONS IN THE OPTIMIZED FOURIER COMPONENTS

We demonstrate that the restored topological phase is stable against small perturbations in the Fourier components of the gate voltages by revisiting the optimized wire of Fig. 4. We start from the optimized Fourier components and add a normally distributed perturbation with zero mean and standard deviation σ_f , drawing 100 different realizations for each value of σ_f . We then use the resulting perturbed Fourier components to compute the gate voltages and the resulting topological gaps $\Delta_{\text{gap}} Q/E_{\text{so}}$, average the topological gaps over the realizations (bottom left panel of Fig. 11), and count which portion of samples is still topological (top left panel). It becomes apparent that for $\sigma_f \leq 1$, almost all cases are still topological in an extended range of parameters [Figs. 11(a)–11(c)]. As a reference, the absolute value of the optimized

Fourier components has mean 1.46 and maximum 5.50 (i.e., $\sigma_f \sim 1$ is indeed a strong perturbation).

In addition, we test the robustness against dysfunctional gates by setting the gate voltage to zero on some gates after the optimization. For this, we repeatedly (100 times) randomly choose a certain percentage of the gates and set their voltages to zero. We then compute the topological gap to see if this destroys the previously restored MZMs again. For the optimized wire of Fig. 4, we find that when 10% of the gates are dysfunctional in over 90% of the cases, the topological phase remains present. Even for 40% still 70% of cases remain topological, however, with a smaller effective gap on average.

APPENDIX F: DEPENDENCE ON THE DISORDER REALIZATION

To demonstrate that the optimization reliably restores the topological phase, we consider several disorder realizations for onsite disorder with strength $\sigma_{\text{dis}} = 25 E_{\text{so}}$ by using different seeds for the random number generator (seed 1 is used in the main text). In the top panel of Fig. 12, we show the topological gap for the disordered wires where all gate voltages are set to zero. At the point of optimization (black square), disorder destroyed the topological phase in four out of five cases (including the main text results), which is a realistic amount of disorder [22].

For a realistic test, we stop optimization after 3000 metric evaluations and use the best gate voltages at this point. In all cases, we find an extended topological phase (center panel) and localized MZMs (lower panel) when using the optimized gate voltages.

-
- [1] T. D. Ladd, F. Jelezko, R. Laflamme, Y. Nakamura, C. Monroe, and J. L. O’Brien, Quantum computers, *Nature (London)* **464**, 45 (2010).
 - [2] C. Kloeffel and D. Loss, Prospects for spin-based quantum computing in quantum dots, *Annu. Rev. Condens. Matter Phys.* **4**, 51 (2013).
 - [3] L. M. K. Vandersypen, H. Bluhm, J. S. Clarke, A. S. Dzurak, R. Ishihara, A. Morello, D. J. Reilly, L. R. Schreiber, and M. Veldhorst, Interfacing spin qubits in quantum dots and donors—hot, dense, and coherent, *npj Quant. Inf.* **3**, 34 (2017).
 - [4] J. Alicea, Y. Oreg, G. Refael, F. von Oppen, and M. P. A. Fisher, Non-Abelian statistics and topological quantum information processing in 1D wire networks, *Nat. Phys.* **7**, 412 (2011).
 - [5] D. J. Clarke, J. D. Sau, and S. Tewari, Majorana fermion exchange in quasi-one-dimensional networks, *Phys. Rev. B* **84**, 035120 (2011).
 - [6] T. Hyart, B. van Heck, I. C. Fulga, M. Burrello, A. R. Akhmerov, and C. W. J. Beenakker, Flux-controlled quantum computation with Majorana fermions, *Phys. Rev. B* **88**, 035121 (2013).
 - [7] S. D. Sarma, M. Freedman, and C. Nayak, Majorana zero modes and topological quantum computation, *npj Quant. Inf.* **1**, 15001 (2015).
 - [8] D. Aasen, M. Hell, R. V. Mishmash, A. Higginbotham, J. Danon, M. Leijnse, T. S. Jespersen, J. A. Folk, C. M. Marcus, K. Flensberg, and J. Alicea, Milestones toward Majorana-based quantum computing, *Phys. Rev. X* **6**, 031016 (2016).
 - [9] T. Karzig, C. Knapp, R. M. Lutchyn, P. Bonderson, M. B. Hastings, C. Nayak, J. Alicea, K. Flensberg, S. Plugge, Y. Oreg, C. M. Marcus, and M. H. Freedman, Scalable designs for quasiparticle-poisoning-protected topological quantum computation with Majorana zero modes, *Phys. Rev. B* **95**, 235305 (2017).
 - [10] R. M. Lutchyn, E. P. A. M. Bakkers, L. P. Kouwenhoven, P. Krogstrup, C. M. Marcus, and Y. Oreg, Majorana zero modes in superconductor–semiconductor heterostructures, *Nat. Rev. Mater.* **3**, 52 (2018).
 - [11] Y. Oreg and F. von Oppen, Majorana zero modes in networks of Cooper-pair boxes: Topologically ordered states and topological quantum computation, *Annu. Rev. Condens. Matter Phys.* **11**, 397 (2020).
 - [12] M. Mandal, N. C. Drucker, P. Siriviboon, T. Nguyen, T. Boonkird, T. N. Lamichhane, R. Okabe, A. Chotrattanapituk, and M. Li, Topological superconductors from a materials perspective, *Chem. Mater.* **35**, 6184 (2023).
 - [13] S. Vijay and L. Fu, Teleportation-based quantum information processing with Majorana zero modes, *Phys. Rev. B* **94**, 235446 (2016).

- [14] A. Y. Kitaev, Unpaired Majorana fermions in quantum wires, *Phys. Usp.* **44**, 131 (2001).
- [15] R. M. Lutchyn, J. D. Sau, and S. Das Sarma, Majorana fermions and a topological phase transition in semiconductor-superconductor heterostructures, *Phys. Rev. Lett.* **105**, 077001 (2010).
- [16] Y. Oreg, G. Refael, and F. von Oppen, Helical liquids and Majorana bound states in quantum wires, *Phys. Rev. Lett.* **105**, 177002 (2010).
- [17] J. D. Sau, S. Tewari, R. M. Lutchyn, T. D. Stanescu, and S. Das Sarma, Non-Abelian quantum order in spin-orbit-coupled semiconductors: Search for topological Majorana particles in solid-state systems, *Phys. Rev. B* **82**, 214509 (2010).
- [18] H. Zhang, Ö. Gül, S. Conesa-Boj, M. P. Nowak, M. Wimmer, K. Zuo, V. Mourik, F. K. de Vries, J. van Veen, M. W. A. de Moor, J. D. S. Bommer, D. J. van Woerkom, D. Car, S. R. Plissard, E. P. A. M. Bakkers, M. Quintero-Pérez, M. C. Cassidy, S. Koelling, S. Goswami, K. Watanabe *et al.*, Ballistic superconductivity in semiconductor nanowires, *Nat. Commun.* **8**, 16025 (2017).
- [19] S. Ahn, H. Pan, B. Woods, T. D. Stanescu, and S. D. Sarma, Estimating disorder and its adverse effects in semiconductor Majorana nanowires, *Phys. Rev. Mater.* **5**, 124602 (2021).
- [20] S. Das Sarma and H. Pan, Disorder-induced zero-bias peaks in Majorana nanowires, *Phys. Rev. B* **103**, 195158 (2021).
- [21] P. Yu, J. Chen, M. Gomanko, G. Badawy, E. P. A. M. Bakkers, K. Zuo, V. Mourik, and S. M. Frolov, Non-Majorana states yield nearly quantized conductance in proximatized nanowires, *Nat. Phys.* **17**, 482 (2021).
- [22] M. Aghaee, A. Akkala, Z. Alam, R. Ali, A. A. Ramirez, M. Andrzejczuk, A. E. Antipov, P. Aseev, M. Astafev, B. Bauer *et al.*, InAs-Al hybrid devices passing the topological gap protocol, *Phys. Rev. B* **107**, 245423 (2023).
- [23] C. Zeng, G. Sharma, S. Tewari, and T. Stanescu, Partially separated Majorana modes in a disordered medium, *Phys. Rev. B* **105**, 205122 (2022).
- [24] S. D. Sarma, J. D. Sau, and T. D. Stanescu, Spectral properties, topological patches, and effective phase diagrams of finite disordered Majorana nanowires, *Phys. Rev. B* **108**, 085416 (2023).
- [25] S. Takei, B. M. Fregoso, H.-Y. Hui, A. M. Lobos, and S. Das Sarma, Soft superconducting gap in semiconductor Majorana nanowires, *Phys. Rev. Lett.* **110**, 186803 (2013).
- [26] G. Kells, D. Meidan, and P. W. Brouwer, Near-zero-energy end states in topologically trivial spin-orbit coupled superconducting nanowires with a smooth confinement, *Phys. Rev. B* **86**, 100503(R) (2012).
- [27] E. Prada, P. San-Jose, and R. Aguado, Transport spectroscopy of NS nanowire junctions with Majorana fermions, *Phys. Rev. B* **86**, 180503(R) (2012).
- [28] D. Rainis, L. Trifunovic, J. Klinovaja, and D. Loss, Towards a realistic transport modeling in a superconducting nanowire with Majorana fermions, *Phys. Rev. B* **87**, 024515 (2013).
- [29] J. Cayao, E. Prada, P. San-Jose, and R. Aguado, SNS junctions in nanowires with spin-orbit coupling: Role of confinement and helicity on the subgap spectrum, *Phys. Rev. B* **91**, 024514 (2015).
- [30] P. San-Jose, J. Cayao, E. Prada, and R. Aguado, Majorana bound states from exceptional points in non-topological superconductors, *Sci. Rep.* **6**, 21427 (2016).
- [31] J. Chen, P. Yu, J. Stenger, M. Hocevar, D. Car, S. R. Plissard, E. P. A. M. Bakkers, T. D. Stanescu, and S. M. Frolov, Experimental phase diagram of zero-bias conductance peaks in superconductor/semiconductor nanowire devices, *Sci. Adv.* **3**, e1701476 (2017).
- [32] C.-X. Liu, J. D. Sau, T. D. Stanescu, and S. Das Sarma, Andreev bound states versus Majorana bound states in quantum dot-nanowire-superconductor hybrid structures: Trivial versus topological zero-bias conductance peaks, *Phys. Rev. B* **96**, 075161 (2017).
- [33] F. Peñaranda, R. Aguado, P. San-Jose, and E. Prada, Quantifying wave-function overlaps in inhomogeneous Majorana nanowires, *Phys. Rev. B* **98**, 235406 (2018).
- [34] J. Avila, F. Peñaranda, E. Prada, P. San-Jose, and R. Aguado, Non-Hermitian topology as a unifying framework for the Andreev versus Majorana states controversy, *Commun. Phys.* **2**, 133 (2019).
- [35] C.-K. Chiu and S. Das Sarma, Fractional Josephson effect with and without Majorana zero modes, *Phys. Rev. B* **99**, 035312 (2019).
- [36] J. Chen, B. D. Woods, P. Yu, M. Hocevar, D. Car, S. R. Plissard, E. P. A. M. Bakkers, T. D. Stanescu, and S. M. Frolov, Ubiquitous non-Majorana zero-bias conductance peaks in nanowire devices, *Phys. Rev. Lett.* **123**, 107703 (2019).
- [37] B. D. Woods, J. Chen, S. M. Frolov, and T. D. Stanescu, Zero-energy pinning of topologically trivial bound states in multiband semiconductor-superconductor nanowires, *Phys. Rev. B* **100**, 125407 (2019).
- [38] A. Vuik, B. Nijholt, A. R. Akhmerov, and M. Wimmer, Reproducing topological properties with quasi-Majorana states, *SciPost Phys.* **7**, 061 (2019).
- [39] O. A. Awoga, J. Cayao, and A. M. Black-Schaffer, Super-current detection of topologically trivial zero-energy states in nanowire junctions, *Phys. Rev. Lett.* **123**, 117001 (2019).
- [40] O. Dmytruk, D. Loss, and J. Klinovaja, Pinning of Andreev bound states to zero energy in two-dimensional superconductor-semiconductor Rashba heterostructures, *Phys. Rev. B* **102**, 245431 (2020).
- [41] H. Pan and S. Das Sarma, Physical mechanisms for zero-bias conductance peaks in Majorana nanowires, *Phys. Rev. Res.* **2**, 013377 (2020).
- [42] E. Prada, P. San-Jose, M. W. A. de Moor, A. Geresdi, E. J. H. Lee, J. Klinovaja, D. Loss, J. Nygård, R. Aguado, and L. P. Kouwenhoven, From Andreev to Majorana bound states in hybrid superconductor-semiconductor nanowires, *Nat. Rev. Phys.* **2**, 575 (2020).
- [43] M. Valentini, F. Peñaranda, A. Hofmann, M. Brauns, R. Hauschild, P. Krogstrup, P. San-Jose, E. Prada, R. Aguado, and G. Katsaros, Nontopological zero-bias peaks in full-shell nanowires induced by flux-tunable Andreev states, *Science* **373**, 82 (2021).
- [44] H. Zhang, M. W. A. de Moor, J. D. S. Bommer, Di Xu, G. Wang, N. van Loo, C.-X. Liu, S. Gazibegovic, J. A. Logan, D. Car, Roy L. M. Op het Veld, P. J. van Veldhoven, S. Koelling, M. A. Verheijen, M. Pendharkar, D. J. Pennachio, B. Shojaei, J. S. Lee, C. J. Palmstrøm, E. P. A. M. Bakkers *et al.*, Large zero-bias peaks in InSb-Al hybrid semiconductor-superconductor nanowire devices, [arXiv:2101.11456](https://arxiv.org/abs/2101.11456).
- [45] D. Bagrets and A. Altland, Class D spectral peak in Majorana quantum wires, *Phys. Rev. Lett.* **109**, 227005 (2012).

- [46] D. I. Pikulin, J. P. Dahlhaus, M. Wimmer, H. Schomerus, and C. W. J. Beenakker, A zero-voltage conductance peak from weak antilocalization in a Majorana nanowire, *New J. Phys.* **14**, 125011 (2012).
- [47] J. Liu, A. C. Potter, K. T. Law, and P. A. Lee, Zero-bias peaks in the tunneling conductance of spin-orbit-coupled superconducting wires with and without Majorana end-states, *Phys. Rev. Lett.* **109**, 267002 (2012).
- [48] C. Moore, C. Zeng, T. D. Stanescu, and S. Tewari, Quantized zero-bias conductance plateau in semiconductor-superconductor heterostructures without topological Majorana zero modes, *Phys. Rev. B* **98**, 155314 (2018).
- [49] A. M. Whiticar, A. Fornieri, E. C. T. O'Farrell, A. C. C. Drachmann, T. Wang, C. Thomas, S. Gronin, R. Kallaher, G. C. Gardner, M. J. Manfra, C. M. Marcus, and F. Nichele, Coherent transport through a Majorana island in an Aharonov-Bohm interferometer, *Nat. Commun.* **11**, 3212 (2020).
- [50] L. Fu, Electron teleportation via Majorana bound states in a mesoscopic superconductor, *Phys. Rev. Lett.* **104**, 056402 (2010).
- [51] M. Hell, K. Flensberg, and M. Leijnse, Distinguishing Majorana bound states from localized Andreev bound states by interferometry, *Phys. Rev. B* **97**, 161401(R) (2018).
- [52] M. Thamm and B. Rosenow, Transmission amplitude through a Coulomb blockaded Majorana wire, *Phys. Rev. Res.* **3**, 023221 (2021).
- [53] D. I. Pikulin, B. van Heck, T. Karzig, E. A. Martinez, B. Nijholt, T. Laeven, G. W. Winkler, J. D. Watson, S. Heedt, M. Temurhan *et al.*, Protocol to identify a topological superconducting phase in a three-terminal device, [arXiv:2103.12217](https://arxiv.org/abs/2103.12217).
- [54] V. Mourik, K. Zuo, S. M. Frolov, S. R. Plissard, E. P. A. M. Bakkers, and L. P. Kouwenhoven, Signatures of Majorana fermions in hybrid superconductor-semiconductor nanowire devices, *Science* **336**, 1003 (2012).
- [55] A. Das, Y. Ronen, Y. Most, Y. Oreg, M. Heiblum, and H. Shtrikman, Zero-bias peaks and splitting in an Al-InAs nanowire topological superconductor as a signature of Majorana fermions, *Nat. Phys.* **8**, 887 (2012).
- [56] M. T. Deng, C. L. Yu, G. Y. Huang, M. Larsson, P. Caroff, and H. Q. Xu, Anomalous zero-bias conductance peak in a Nb-InSb nanowire-Nb hybrid device, *Nano Lett.* **12**, 6414 (2012).
- [57] F. Nichele, A. C. C. Drachmann, A. M. Whiticar, E. C. T. O'Farrell, H. J. Suominen, A. Fornieri, T. Wang, G. C. Gardner, C. Thomas, A. T. Hatke, P. Krogstrup, M. J. Manfra, K. Flensberg, and C. M. Marcus, Scaling of Majorana zero-bias conductance peaks, *Phys. Rev. Lett.* **119**, 136803 (2017).
- [58] L. P. Rokhinson, X. Liu, and J. K. Furdyna, The fractional a.c. Josephson effect in a semiconductor-superconductor nanowire as a signature of Majorana particles, *Nat. Phys.* **8**, 795 (2012).
- [59] S. M. Albrecht, A. P. Higginbotham, M. Madsen, F. Kuemmeth, T. S. Jespersen, J. Nygård, P. Krogstrup, and C. M. Marcus, Exponential protection of zero modes in Majorana islands, *Nature (London)* **531**, 206 (2016).
- [60] A. Fornieri, A. M. Whiticar, F. Setiawan, E. Portolés, A. C. C. Drachmann, A. Keselman, S. Gronin, C. Thomas, T. Wang, R. Kallaher *et al.*, Evidence of topological superconductivity in planar Josephson junctions, *Nature (London)* **569**, 89 (2019).
- [61] S. Vaitiekėnas, G. W. Winkler, B. Van Heck, T. Karzig, M.-T. Deng, K. Flensberg, L. I. Glazman, C. Nayak, P. Krogstrup, R. M. Lutchyn, and C. M. Marcus, Flux-induced topological superconductivity in full-shell nanowires, *Science* **367**, eaav3392 (2020).
- [62] S. Vaitiekėnas, Y. Liu, P. Krogstrup, and C. M. Marcus, Zero-bias peaks at zero magnetic field in ferromagnetic hybrid nanowires, *Nat. Phys.* **17**, 43 (2021).
- [63] A. Banerjee, O. Lesser, M. A. Rahman, H. R. Wang, M.-R. Li, A. Kringhøj, A. M. Whiticar, A. C. C. Drachmann, C. Thomas, T. Wang, M. J. Manfra, E. Berg, Y. Oreg, A. Stern, and C. M. Marcus, Signatures of a topological phase transition in a planar Josephson junction, *Phys. Rev. B* **107**, 245304 (2023).
- [64] M. C. Dartailh, W. Mayer, J. Yuan, K. S. Wickramasinghe, A. Matos-Abiague, I. Žutić, and J. Shabani, Phase signature of topological transition in Josephson junctions, *Phys. Rev. Lett.* **126**, 036802 (2021).
- [65] J. J. Cuzzo, W. Pan, J. Shabani, and E. Rossi, Microwave-tunable diode effect in asymmetric SQUIDs with topological Josephson junctions, [arXiv:2303.16931](https://arxiv.org/abs/2303.16931).
- [66] J. Klinovaja, P. Stano, and D. Loss, Transition from fractional to Majorana fermions in Rashba nanowires, *Phys. Rev. Lett.* **109**, 236801 (2012).
- [67] S. Boutin, J. Camirand Lemyre, and I. Garate, Majorana bound state engineering via efficient real-space parameter optimization, *Phys. Rev. B* **98**, 214512 (2018).
- [68] N. Mohanta, T. Zhou, J.-W. Xu, J. E. Han, A. D. Kent, J. Shabani, I. Žutić, and A. Matos-Abiague, Electrical control of Majorana bound states using magnetic stripes, *Phys. Rev. Appl.* **12**, 034048 (2019).
- [69] S. Turcotte, S. Boutin, J. C. Lemyre, I. Garate, and M. Pioro-Ladrière, Optimized micromagnet geometries for Majorana zero modes in low g -factor materials, *Phys. Rev. B* **102**, 125425 (2020).
- [70] A. Melo, T. Tanev, and A. R. Akhmerov, Greedy optimization of the geometry of Majorana Josephson junctions, *SciPost Phys.* **14**, 047 (2023).
- [71] Ö. Gül, D. J. van Woerkom, I. van Weperen, D. Car, S. R. Plissard, E. P. A. M. Bakkers, and L. P. Kouwenhoven, Towards high mobility InSb nanowire devices, *Nanotechnology* **26**, 215202 (2015).
- [72] O. A. Awoga, J. Cayao, and A. M. Black-Schaffer, Robust topological superconductivity in weakly coupled nanowire-superconductor hybrid structures, *Phys. Rev. B* **105**, 144509 (2022).
- [73] O. A. Awoga, M. Leijnse, A. M. Black-Schaffer, and J. Cayao, Mitigating disorder-induced zero-energy states in weakly-coupled semiconductor-superconductor hybrid systems, *Phys. Rev. B* **107**, 184519 (2023).
- [74] M. Thamm and B. Rosenow, Machine learning optimization of Majorana hybrid nanowires, *Phys. Rev. Lett.* **130**, 116202 (2023).
- [75] F. Arute, K. Arya, R. Babbush, D. Bacon, J. C. Bardin, R. Barends, R. Biswas, S. Boixo, Fernando G. S. L. Brandao, D. A. Buell, B. Burkett, Y. Chen, Z. Chen, B. Chiaro, R. Collins, W. Courtney, A. Dunsworth, E. Farhi, B. Foxen, A. Fowler *et al.*, Quantum supremacy using a programmable superconducting processor, *Nature (London)* **574**, 505 (2019).
- [76] D. T. Lennon, H. Moon, L. C. Camenzind, L. Yu, D. M. Zumbühl, G. A. D. Briggs, M. A. Osborne, E. A. Laird, and N. Ares, Efficiently measuring a quantum device using machine learning, *npj Quant. Inf.* **5**, 79 (2019).

- [77] N. Ares, Machine learning as an enabler of qubit scalability, *Nat. Rev. Mater.* **6**, 870 (2021).
- [78] T. A. Baart, P. T. Eendebak, C. Reichl, W. Wegscheider, and L. M. K. Vandersypen, Computer-automated tuning of semiconductor double quantum dots into the single-electron regime, *Appl. Phys. Lett.* **108**, 213104 (2016).
- [79] T. Botzem, M. D. Shulman, S. Foletti, S. P. Harvey, O. E. Dial, P. Bethke, P. Cerfontaine, R. P. G. McNeil, D. Mahalu, V. Umansky, A. Ludwig, A. Wieck, D. Schuh, D. Bougeard, A. Yacoby, and H. Bluhm, Tuning methods for semiconductor spin qubits, *Phys. Rev. Appl.* **10**, 054026 (2018).
- [80] S. S. Kalantre, J. P. Zwolak, S. Ragole, X. Wu, N. M. Zimmerman, M. D. Stewart, and J. M. Taylor, Machine learning techniques for state recognition and auto-tuning in quantum dots, *npj Quant. Inf.* **5**, 6 (2019).
- [81] J. D. Teske, S. S. Humpohl, R. Otten, P. Bethke, P. Cerfontaine, J. Dedden, A. Ludwig, A. D. Wieck, and H. Bluhm, A machine learning approach for automated fine-tuning of semiconductor spin qubits, *Appl. Phys. Lett.* **114**, 133102 (2019).
- [82] A. R. Mills, M. M. Feldman, C. Monical, P. J. Lewis, K. W. Larson, A. M. Mounce, and J. R. Petta, Computer-automated tuning procedures for semiconductor quantum dot arrays, *Appl. Phys. Lett.* **115**, 113501 (2019).
- [83] R. Durrer, B. Kratochwil, J. V. Koski, A. J. Landig, C. Reichl, W. Wegscheider, T. Ihn, and E. Greplova, Automated tuning of double quantum dots into specific charge states using neural networks, *Phys. Rev. Appl.* **13**, 054019 (2020).
- [84] H. Moon, D. T. Lennon, J. Kirkpatrick, N. M. van Esbroeck, L. C. Camenzind, L. Yu, F. Vigneau, D. M. Zumbühl, G. A. D. Briggs, M. A. Osborne, D. Sejdinovic, E. A. Laird, and N. Ares, Machine learning enables completely automatic tuning of a quantum device faster than human experts, *Nat. Commun.* **11**, 4161 (2020).
- [85] N. M. van Esbroeck, D. T. Lennon, H. Moon, V. Nguyen, F. Vigneau, L. C. Camenzind, L. Yu, D. M. Zumbühl, G. A. D. Briggs, D. Sejdinovic, and N. Ares, Quantum device fine-tuning using unsupervised embedding learning, *New J. Phys.* **22**, 095003 (2020).
- [86] D. L. Craig, H. Moon, F. Fedele, D. T. Lennon, B. van Straaten, F. Vigneau, L. C. Camenzind, D. M. Zumbühl, G. A. D. Briggs, M. A. Osborne, D. Sejdinovic, and N. Ares, Bridging the reality gap in quantum devices with physics-aware machine learning, *Phys. Rev. X* **14**, 011001 (2024).
- [87] F. Fedele, A. Chatterjee, S. Fallahi, G. C. Gardner, M. J. Manfra, and F. Kuemmeth, Simultaneous operations in a two-dimensional array of singlet-triplet qubits, *PRX Quant.* **2**, 040306 (2021).
- [88] J. Ziegler, T. McJunkin, E. S. Joseph, S. S. Kalantre, B. Harpt, D. E. Savage, M. G. Lagally, M. A. Eriksson, J. M. Taylor, and J. P. Zwolak, Toward robust autotuning of noisy quantum dot devices, *Phys. Rev. Appl.* **17**, 024069 (2022).
- [89] O. Krause, A. Chatterjee, F. Kuemmeth, and E. van Nieuwenburg, Learning Coulomb diamonds in large quantum dot arrays, *SciPost Phys.* **13**, 084 (2022).
- [90] A. Frees, J. K. Gamble, D. R. Ward, R. Blume-Kohout, M. A. Eriksson, M. Friesen, and S. N. Coppersmith, Compressed optimization of device architectures for semiconductor quantum devices, *Phys. Rev. Appl.* **11**, 024063 (2019).
- [91] H.-C. Ruiz Euler, M. N. Boon, J. T. Wildeboer, B. van de Ven, T. Chen, H. Broersma, P. A. Bobbert, and W. G. van der Wiel, A deep-learning approach to realizing functionality in nanoelectronic devices, *Nat. Nanotechnol.* **15**, 992 (2020).
- [92] N. Hansen, The CMA evolution strategy: A tutorial, [arXiv:1604.00772](https://arxiv.org/abs/1604.00772).
- [93] M. Thamm and B. Rosenow, Code: Conductance based machine learning of optimal gate voltages for disordered Majorana wires, Zenodo, doi:[10.5281/zenodo.8417636](https://doi.org/10.5281/zenodo.8417636).
- [94] J. Danon, A. B. Hellenes, E. B. Hansen, L. Casparis, A. P. Higginbotham, and K. Flensberg, Nonlocal conductance spectroscopy of Andreev bound states: Symmetry relations and BCS charges, *Phys. Rev. Lett.* **124**, 036801 (2020).
- [95] A. R. Akhmerov, J. P. Dahlhaus, F. Hassler, M. Wimmer, and C. W. J. Beenakker, Quantized conductance at the Majorana phase transition in a disordered superconducting wire, *Phys. Rev. Lett.* **106**, 057001 (2011).
- [96] N. Hansen, The CMA evolution strategy: A comparing review, in *Towards a New Evolutionary Computation, Studies in Fuzziness and Soft Computing*, edited by J. A. Lozano, E. Bengoetxea, I. Inza, and P. Larrañaga (Springer-Verlag, Berlin, 2006), pp. 75–102.
- [97] J. A. Lozano, E. Bengoetxea, I. Inza, and P. Larrañaga, eds., *Towards a New Evolutionary Computation: Advances in the Estimation of Distribution Algorithms*, Studies in Fuzziness and Soft Computing, Vol. 192 (Springer-Verlag, Berlin, Heidelberg, 2006).
- [98] I. Loshchilov and F. Hutter, CMA-ES for hyperparameter optimization of deep neural networks, [arxiv:1604.07269](https://arxiv.org/abs/1604.07269).
- [99] M. Willjuice Iruthayarajan and S. Baskar, Covariance matrix adaptation evolution strategy based design of centralized PID controller, *Expert Syst. Appl.* **37**, 5775 (2010).
- [100] I. Loshchilov, M. Schoenauer, and M. Sebag, in *Proceedings of the 15th Annual Conference Companion on Genetic and Evolutionary Computation* (Association for Computing Machinery, New York, 2013), pp. 1177–1184.
- [101] C. W. Groth, M. Wimmer, A. R. Akhmerov, and X. Waintal, Kwant: A software package for quantum transport, *New J. Phys.* **16**, 063065 (2014).
- [102] G. W. Winkler, A. E. Antipov, B. van Heck, A. A. Soluyanov, L. I. Glazman, M. Wimmer, and R. M. Lutchyn, Unified numerical approach to topological semiconductor-superconductor heterostructures, *Phys. Rev. B* **99**, 245408 (2019).
- [103] A. Pöschl, Nonlocal Transport Signatures of Andreev Bound States, Ph.D. thesis, Center for Quantum Devices, Niels Bohr Institute, University of Copenhagen, [arXiv:2212.12068](https://arxiv.org/abs/2212.12068) (2022).
- [104] R. Hess, H. F. Legg, D. Loss, and J. Klinovaja, Trivial Andreev band mimicking topological bulk gap reopening in the nonlocal conductance of long Rashba nanowires, *Phys. Rev. Lett.* **130**, 207001 (2023).
- [105] S. D. Sarma and H. Pan, Disorder effects on the so-called Andreev band in Majorana nanowires, [arXiv:2306.10041](https://arxiv.org/abs/2306.10041).
- [106] R. Hess, H. F. Legg, D. Loss, and J. Klinovaja, Reply to “comment on ‘trivial Andreev band mimicking topological bulk gap reopening in the nonlocal conductance of long Rashba nanowires,’” [arXiv:2306.16853](https://arxiv.org/abs/2306.16853).
- [107] A. Antipov, W. Cole, K. Kalashnikov, F. Karimi, R. Lutchyn, C. Nayak, D. Pikulin, and G. Winkler, Comment on Hess *et al.* *Phys. Rev. Lett.* **130**, 207001 (2023), [arXiv:2307.15813](https://arxiv.org/abs/2307.15813).

- [108] J. Cayao and P. Buset, Confinement-induced zero-bias peaks in conventional superconductor hybrids, *Phys. Rev. B* **104**, 134507 (2021).
- [109] Nikolaus Hansen, yoshihikoueno, ARF1, Kento Nozawa, Matthew Chan, Youhei Akimoto, and Dimo Brockhoff, *CMA-ES/pycma: r3.1.0* (Zenodo, 2021), <https://zenodo.org/records/5002422>.
- [110] E. A. Lynton, B. Serin, and M. Zucker, The superconductive critical temperature and the electronic specific heat of impure tin, *J. Phys. Chem. Solids* **3**, 165 (1957).
- [111] A. B. Pippard, The effect of alloying on the superconducting transition temperature of tin, *J. Phys. Chem. Solids* **3**, 175 (1957).
- [112] P. W. Anderson, Theory of dirty superconductors, *J. Phys. Chem. Solids* **11**, 26 (1959).
- [113] L. J. Buchholtz and G. Zwicknagl, Identification of *p*-wave superconductors, *Phys. Rev. B* **23**, 5788 (1981).
- [114] P. Hirschfeld, D. Vollhardt, and P. Wölfle, Resonant impurity scattering in heavy fermion superconductors, *Solid State Commun.* **59**, 111 (1986).
- [115] S. Schmitt-Rink, K. Miyake, and C. M. Varma, Transport and thermal properties of heavy-fermion superconductors: A unified picture, *Phys. Rev. Lett.* **57**, 2575 (1986).
- [116] K. Maki and E. Puchkaryov, Impurity scattering in isotropic *p*-wave superconductors, *Europhys. Lett.* **45**, 263 (1999).